Three Dimensional Carbon-Nanotube Polymers

Zhisheng Zhao,[†] Bo Xu,[†] Li-Min Wang,[†] Xiang-Feng Zhou,[‡] Julong He,[†] Zhongyuan Liu,[†] Hui-Tian Wang,[‡] and Yongjun Tian[†,*]

[†]State Key Laboratory of Metastable Materials Science and Technology, Yanshan University, Qinhuangdao 066004, China, and [‡]School of Physics and Key Laboratory of Weak-Light Nonlinear Photonics, Ministry of Education, Nankai University, Tianjin 300071, China

ABSTRACT Eight fascinating sp^2- and sp^3-hybridized carbon allotropes have been uncovered using a newly developed *ab initio* particle-swarm optimization methodology for crystal structure prediction. These crystalline allotropes can be viewed respectively as three-dimensional (3D) polymers of (4,0), (5,0), (7,0), (8,0), (9,0), (3,3), (4,4), and (6,6) carbon nanotubes, termed 3D-(*n*, 0) or 3D-(*n*, *n*) carbons. The ground-state energy calculations show that the carbons all have lower energies than C_{60} fullerene, and some are energetically more stable than the *van der Waals* packing configurations of their nanotube parents. Owing to their unique configurations, they have distinctive electronic properties, high Young's moduli, high tensile strength, ultrahigh hardness, good ductility, and low density, and may be potentially applied to a variety of needs.

KEYWORDS: 3D nanotube polymers · low energy · low density · distinctive electronic properties · superior mechanical properties

Carbon exists in various fascinating and aesthetically pleasing architectures due to its ability to form sp-, sp^2-, and sp^3-hybridized bonds, fostering graphite, diamond, hexagonal diamond (lonsdaleite), carbine, chaoite, amorphous carbon, nanotubes, fullerenes, graphene, and so on. These carbon allotropes possess outstanding and unparalleled properties, as well as unique scientific and technological importance, such that searching for new carbon allotropes has long been a hot topic in scientific research communities.

Graphite is known to be the most thermodynamically stable carbon configuration at ambient conditions. To promote the transition from graphite to other carbon allotropes, external energies are needed. Thus far, many experimental technologies can achieve these transformations. For example, high-pressure and high-temperature methods for the synthesis of diamond and hexagonal diamond,[1,2] laser vaporization of graphite to form fullerenes and carbon chain molecules,[3,4] pulsed laser deposition for synthesis of amorphous carbon,[5,6] and mechanical peeling to obtain graphene[7,8] have all been achieved. Physical and chemical reprocessing of the metastable carbon phases obtained, such as amorphous carbon, fullerenes, and nanotubes, was considered as an alternative and promising route for the synthesis of new carbon phases with novel electronic and mechanical properties. In the past three decades, some interesting carbon phases were successfully and artificially created, for example, body-centered cubic (bcc) carbon,[9,10] one-dimensional (1D) orthorhombic, two-dimensional (2D) tetragonal (and rhombohedral), superhard three-dimensional (3D) polymeric phases of C_{60},[11−15] and some undetermined carbon phases originating from fullerenes and nanotubes.[15−18]

To identify new carbon phases in conventional experiments, researchers can suffer a number of difficulties because small new phases are often concealed in large amounts of the known phases of many products (*e.g.*, raw material, generative graphite, and amorphous carbon).[1−8,11−18] Corresponding theoretical designs are thus necessary as a powerful tool for explaining experimental phenomena or predicting novel viable carbon phases. Recently, theoretically simulative monoclinic carbon (*M*-carbon), body-centered tetragonal C_4 (bct-carbon), and orthorhombic carbon (*W*-carbon) were suggested as candidate structures of transparent superhard carbon phases experimentally produced by the cold compression of graphite.[19−23] A honeycomb hexagonal carbon structure was used to interpret a superhard carbon, which was experimentally recovered from cold compression of carbon nanotubes.[17,24] Quite noticeable is that bct-carbon actually consists of interconnected armchair (2,2) nanotubes, as obtained early on by the theoretical compression of armchair (10, 10) nanotubes;[25] and this honeycomb hexagonal carbon essentially derives from a 3D polymer of zigzag (6,0) nanotubes.[26] Therefore, here we call them 3D-(2,2) carbon and 3D-(6,0) carbon, respectively.

In view of significant progress in the latest calculation methods, such as metadynamics,[27−29] evolutionary algorithm,[30−33] random sampling,[34−36] and particle-swarm

* Address correspondence to fhcl@ysu.edu.cn.

Received for review June 3, 2011 and accepted August 12, 2011.

Published online August 12, 2011
10.1021/nn202053t

optimization (PSO) algorithm,[37−39] the crystal structures of materials can now be forecasted with high accuracy without requiring any experimental data. In this work, we focus on such a class of 3D carbon nanotube polymers, and eight novel carbon allotropes are predicted using a new *ab initio* PSO algorithm.[37−39] These allotropes, called 3D-(*n*, 0) and 3D-(*n*, *n*) carbons, originate from 3D polymers of zigzag (4,0), (5,0), (7,0), (8,0), (9,0), and armchair (3,3), (4,4), (6,6) carbon nanotubes, respectively. All of them have lower ground-state energies than C_{60} fullerene, and some are energetically more stable than their nanotube parents. Specifically, the exotic structural, electronic, and mechanical properties of these carbons are discussed.

RESULTS AND DISCUSSION

Structural Properties. Figure 1 shows the artistic crystal structures of 3D-(*n*, 0) or 3D-(*n*, *n*) carbon allotropes. The building principle of all structures is perfect junctions by shared-wall identical nanotubes. The junctions are formed by diamond-like sp^3 bond buckling, while shared walls consist of flattened sp^2-hybridized graphene sheets. Flattened graphene sections without wall-curvature energies are more stable than the circular surfaces of nanotubes and fullerenes, which are responsible for the preference of such building constructions. The 3D-(*n*, 0) carbons can be viewed as seamless interlinks of corresponding zigzag (*n*, 0) nanotubes, while armchair (*n*, *n*) nanotubes make up of 3D-(*n*, *n*) carbons with seams. In 3D-(3,3) and 3D-(4,4) carbons, the seams are square four-atom rings; in 3D-(6,6) carbon, there are trigonal three-atom rings. The details of the crystal structures, including their space group, lattice parameters, and atomic positions, are shown in Supporting Information (Table S1).

Based on these configurations, a notable feature is the low density of the carbon allotropes, which are intuitively porous along their axial directions. 3D-(4,4) and 3D-(6,0) carbons have densities comparable with that of graphite (2.295 $g \cdot cm^{-3}$), and 3D-(9,0) and 3D-(6,6) carbons have the lowest densities with respective values of 1.902 and 1.720 $g \cdot cm^{-3}$. The densities of other 3D-(*n*, 0) or 3D-(*n*, *n*) carbons are just between those of diamond (3.633 $g \cdot cm^{-3}$) and graphite (Table 1). Interstitial sites in these structures could accommodate other species, such as hydrogen and alkali metals. Such carbons have potential applications as shape-selective catalysts, molecular sieves, and absorbents.

Thermodynamics Stability. Figure 2 shows the computed ground-state energy differences of C_{60}, (*n*, 0) or (*n*, *n*) carbon nanotubes, and 3D-(*n*, 0) or 3D-(*n*, *n*) carbon allotropes, relative to graphite, respectively. In the current study, the crystal structures of experimental low-temperature ordered C_{60} phase,[40] and periodic hexagonal-lattice nanotubes (building principles see Methods) were used to calculate their ground-state

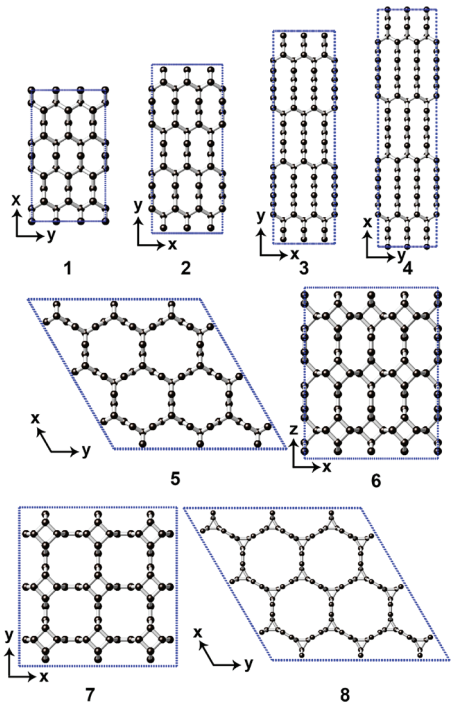

Figure 1. Top views of novel 3D-(*n*, 0) or 3D-(*n*, *n*) carbons along their axial directions. 1−8:2 × 3 × 1 supercell of 3D-(4,0) carbon, 3 × 2 × 1 supercell of 3D-(5,0) carbon, 3 × 2 × 1 supercell of 3D-(7,0) carbon, 2 × 3 × 1 supercell of 3D-(8,0) carbon, 3 × 3 × 1 supercell of 3D-(9,0) carbon, 2 × 1 × 3 supercell of 3D-(3,3) carbon, 3 × 3 × 1 supercell of 3D-(4,4) carbon, and 3 × 3 × 1 supercell of 3D-(6,6) carbon, respectively. The black arrows and their directions indicate the corresponding x, y, z axes of crystal structures.

TABLE 1. The density ($g \cdot cm^{-3}$), axial Young's moduli Y_a (TPa), radial Young's moduli Y_r (TPa), axial tensile strength σ_a (GPa), radial tensile strength σ_r (GPa), bulk moduli *B* (GPa), shear moduli *G* (GPa), *B*/*G* ratio, and Vickers hardness *H* (GPa) of 3D naonotube polymers

Carbon	Density	Y_a	Y_r	σ_a	σ_r	*B*	*G*	*B*/*G*	*H*
3D-(3,0)	3.623	1.241	1.374	95.38	100.91	454.5	551.2	0.82	96.9
3D-(4,0)	3.314	1.284	0.636	142.28	69.44	372.8	372.2	1.00	56.8
3D-(5,0)	3.200	1.226	0.553	160.18	50.52	352.5	285.5	1.23	40.9
3D-(6,0)	2.448, 2.449[a]	0.957	0.449	53.10	74.31	274.1	243.1	1.13	54.9
3D-(7,0)	3.020	1.184	0.220	174.82	31.82	273.9	201.6	1.36	49.8
3D-(8,0)	2.944	1.212	0.299	177.19	26.70	280.6	198.3	1.42	54.5
3D-(9,0)	1.902	0.740	0.094	119.01	51.53	207.7	101.5	2.05	36.0
3D-(2,2)	3.438	1.243	0.943	112.36	93.80	420.1, 428.7[b]	427.1, 427[c]	0.98	92.6
3D-(3,3)	3.054	1.133	0.487	129.98	76.54	343.9	283.5	1.21	90.9
3D-(4,4)	2.404	0.925	0.565	114.05	115.09	277.6	140.4	1.98	79.8
3D-(6,6)	1.720	0.678	0.092	83.13	50.79	195.4	94.1	2.08	46.7

[a] Reference 24. [b] Reference 21. [c] Reference 22.

energies. The 3D-(*n*, 0) or 3D-(*n*, *n*) carbon allotropes we investigated also include previously proposed sp^3-hybridized 3D-(2,2) carbon,[21,22,25] sp^2- and sp^3-hybridized 3D-(6,0) carbon,[24,26] and sp^3-hybridized hexagonal diamond [*viz*. 3D-(3,0) carbon]. Figure 2 shows that well-known carbon nanotubes, C_{60}, and the 3D-(*n*, 0) or

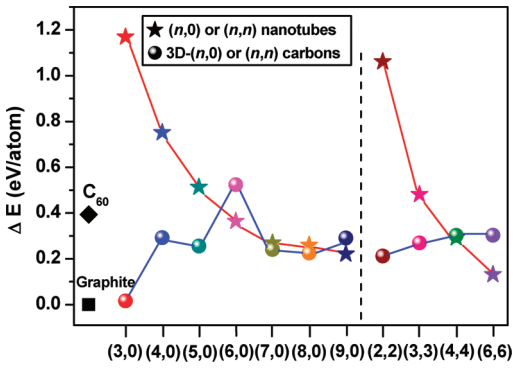

Figure 2. The computed ground-state energy differences of 3D nanotube polymers, relative to graphite.

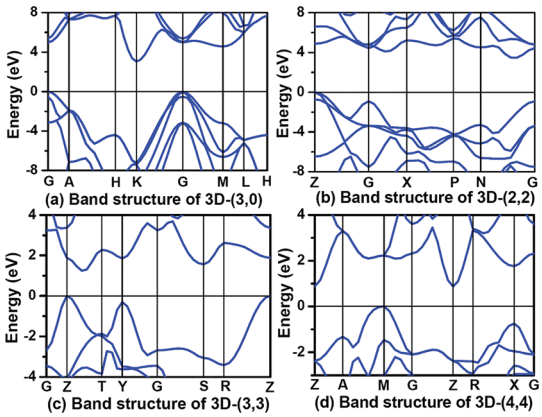

Figure 3. Band structures of semiconducting 3D-(*n*, 0) or 3D-(*n*, *n*) carbons.

3D-(*n*, *n*) carbon allotropes all have energies higher than graphite, specifically indicating their metastability. The energy difference between C_{60} and graphite is 0.393 eV/atom, compared with other calculated value (0.387 eV/atom).[41] The energy difference between the (7,0) nanotube and graphite is 0.241 eV/atom, compared with other calculated value (0.25 eV/atom).[21] As seen from Figure S1 (Supporting Information), smaller nanotubes have larger bending bond angles at the corners of a curved graphene sheet, which result in higher energies (Figure 2). Even so, experimental evidence still shows that the smallest zigzag (4,0) and smallest armchair (2,2) nanotubes can be grown from a larger nanotube and inside a multiwalled carbon nanotube, respectively.[42,43] In the eleven 3D nanotube polymers considered in this work, the 3D-(6,0) carbon has the highest energy, the 3D-(3,0) carbon has the lowest energy, and other polymers have close energies. Of these, all the carbons, except the previously proposed 3D-(6,0) carbon, have lower energies than C_{60}; 3D-(3,0), 3D-(4,0), 3D-(5,0), 3D-(7,0), 3D-(8,0), 3D-(2,2), and 3D-(3,3) carbon allotropes all have lower energies than their corresponding nanotubes parents. Because of the low energies of the 3D-(*n*, 0) or 3D-(*n*, *n*) carbon allotropes, it is highly worth testing to synthesize them through dealing with high-energy carbon nanotubes and/or fullerenes.

Electronic Properties. We first studied the peculiar electronic properties of 3D nanotube polymers and compared them with their corresponding nanotube parents. Previous experimental results demonstrate that zigzag nanotubes have band gaps with magnitudes that depend inversely on the square of the tube radius, whereas isolated armchair nanotubes are all metallic.[44,45] According to the relations of band gaps and tube radii,[44,45] the band gaps of zigzag (3,0), (4,0), (5,0), (6,0), (7,0), (8,0) and (9,0) nanotubes are 0.72, 0.41, 0.26, 0.18, 0.13, 0.10, and 0.08 eV, respectively.

All the seven 3D-(*n*, 0) carbons investigated, except the 3D-(3,0) carbon, are conducting, distinct from their semiconducting zigzag nanotube parents. Four 3D-(*n*, *n*) carbons studied, except the 3D-(6,6) carbon, are semiconducting, unlike their metallic armchair nanotube parents. Therefore, from nanotubes to 3D nanotube polymers, changes in conduction properties may occur. Through a detailed analysis of band structures (see Figure 3, Figure 4, and Supporting Information, Figure S2), 3D-(3,0), 3D-(2,2), 3D-(3,3), and 3D-(4,4) carbons have respective band gaps of 3.05, 3.52, 1.21, and 0.93 eV; 3D-(4,0), 3D-(6,0), and 3D-(6,6) carbons are semimetallic according to the suggested standard,[46] and 3D-(5,0), 3D-(7,0), 3D-(8,0), and 3D-(9,0) carbons are metallic. Because density functional theory (DFT) can systematically underestimate the band gaps by about 30%−40%, semiconducting 3D nanotube polymers would have larger band gaps. Because semimetallic polymers have fewer charge carriers than metallic polymers, they typically have lower electrical and thermal conductivity.

We combined the electron orbits and local density of states (LDOS) (see Figure 4, Figure 5, and Figure S2) to explain the unusual conducting directions of semimetallic and metallic 3D nanotube polymers. This is a key for understanding which atoms in a crystal would give contributions at the Fermi level and bring about conductivity (see LDOS in Figure 5 and Figure S2). For 3D-(4,0), 3D-(5,0), 3D-(6,0), 3D-(7,0), 3D-(8,0), and 3D-(9,0) carbons, almost all the conducting electrons at the Fermi level come from the $2p_z$ orbits of sp^2 bonded carbon atoms (green, olive, and dark olive atoms in crystal structures) without the contributions of sp^3 bonded atoms (red atoms). However, both sp^2 and sp^3 bonded atoms in the 3D-(6,6) carbon contribute at the Fermi level. Further studies of electron orbits can describe the directional movements of excited electrons under varying electric fields or temperatures. It is known that each energy band is defined by the position of its eigenvalue in the ordered list of electronic energies at each *k*-point; and the corresponding electron orbit is the square of the absolute value of the wave function for this given electronic band, summed over all *k*-points. Here, our drawn electron orbits are the summations from the blue

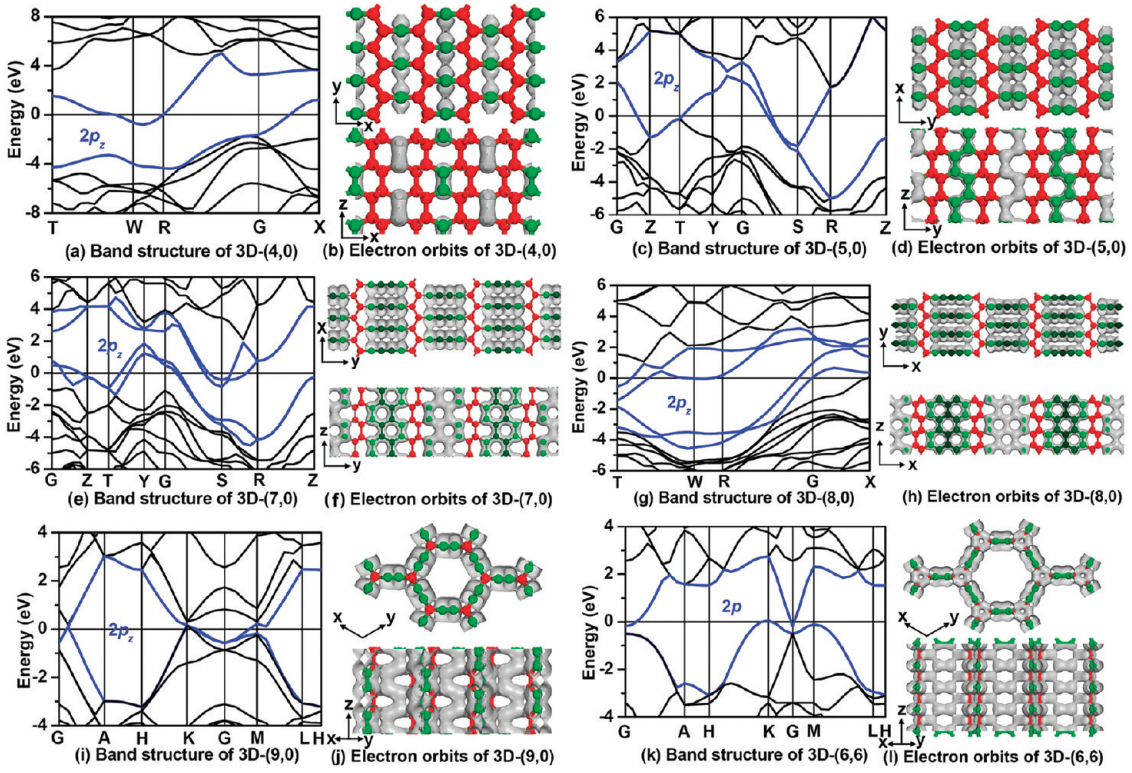

Figure 4. Band structures and electron orbits of conducting 3D-(*n*, 0) or 3D-(*n*, *n*) carbons. The green, red, olive, and dark olive atoms are corresponding to different atomic positions of crystal structures. Red atoms are sp^3 hybridized, and green (or olive) atoms are sp^2 hybridized. The gray parts represent the electron orbits.

bands (Figure 4) near the Fermi level. Every electron orbit figure includes two projections of electron orbit: upper and lower projections are two top views along the axial and radial directions of the crystal structure, respectively. Because of the short distance (about $(3)^{1/2}$ bond length of diamond) between adjacent flattened graphene sections, the $2p_z$ orbits of sp^2 bonded atoms of 3D-(*n*, 0) carbon (*n* = 4, 5, 6, 7, 8, and 9) are overlapped and form the π bonds (see upper projections). Moreover, their corresponding electron orbits do not appear in sp^3 bonded atoms, so the sp^3 bonded atoms are not conductive, which is consistent with the results of LDOS. Consequently, 3D-(4,0) carbon is conductive in the *y*-axes, but its conductivity is interrupted in the *x*- and *z*-axes; 3D-(5,0) carbon is conductive in the *xz* plane, but its conductivity is interrupted in the *y*-axes; 3D-(6,0) carbon is conductive in the *xy* plane, but its conductivity is interrupted in the *z*-axes; 3D-(7,0) carbon is conductive in the *xz* plane, but its conductivity is interrupted in the *y*-axes; 3D-(8,0) carbon is conductive in the *yz* plane, but its conductivity is interrupted in the *x*-axes; and 3D-(9,0) carbon is 3D conductive. Although the 3D-(6,6) carbon is 3D conductive, its conducting electrons partially come from sp^3 bonded atoms. Its blue bands near the Fermi level are the results of hybridization of the $2p_z$ orbits of sp^2 bonded atoms and the hybridized orbits of sp^3 bonded atoms. In short, 3D-(4,0) carbon has a linear conductivity; 3D-(5,0), 3D-(6,0), 3D-(7,0), and 3D-(8,0) carbons have planar conductivity; and 3D-(9,0) and 3D-(6,6) carbons are 3D conductive.

The carbons from 3D-(4,0) to 3D-(9,0) are all conductive because their bands pass through the Fermi level (see Figure 4 and Figure S2). However, the conductivities of these carbons show unusual variations due to the different sp^2/sp^3 ratios and the varied sp^2 bond distributions in the crystal structures. In the 3D-(*n*, 0) carbons, the sp^2/sp^3 ratios are calculated as the sp^2 and sp^3 hybridized bond numbers per unit cell (see Supporting Information, Figure S3). The sp^2/sp^3 ratios of the 3D-(4,0), 3D-(5,0), 3D-(6,0), 3D-(7,0), 3D-(8,0), and 3D-(9,0) carbons are 2/20, 8/20, 3/14, 20/20, 26/20, and 12/14, respectively. The sp^2 bonds are distributed in isolation for the 3D-(4,0) and 3D-(6,0) carbons, in zigzag chains for the 3D-(5,0) and 3D-(9,0) carbons, in zigzag hexagons for the 3D-(7,0) carbon, and in three-hexagon chains for the 3D-(8,0) carbon (see Figure S3). The p_z electrons are basically localized in the 3D-(4,0) and 3D-(6,0) carbons, in contrast to the gradually delocalized p_z electrons in the 3D-(5,0), 3D-(9,0), 3D-(7,0), and 3D-(8,0) carbons. Compared with the 3D-(4,0) and 3D-(6,0) carbons, the 3D-(5,0) and 3D-(9,0) carbons have two steeper bands across the Fermi level (blue bands in Figure 4), indicating higher conduction electron velocities. Compared with the 3D-(4,0), 3D-(6,0), 3D-(5,0) and 3D-(9,0) carbons, the 3D-(7,0) and 3D-(8,0) carbons have four steep bands across the Fermi level (blue bands in Figure 4),

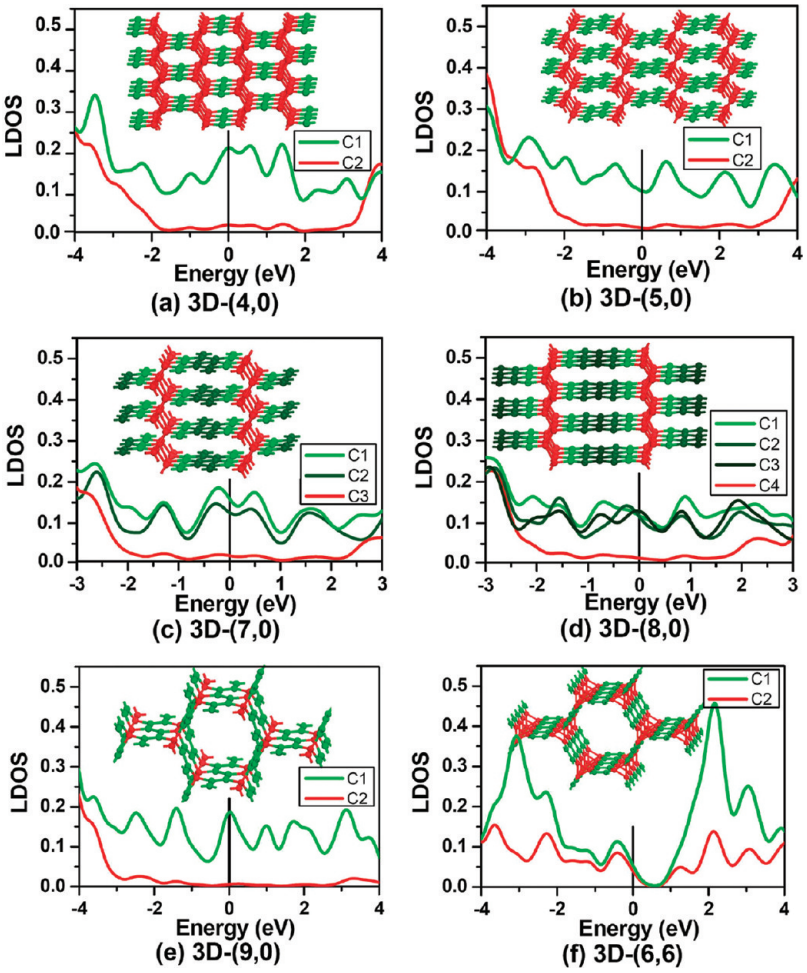

Figure 5. Local density of states (LDOS) (electrons/eV·per atom) of conducting 3D-(*n*, 0) or 3D-(*n*, *n*) carbons. Green, red, olive, and dark olive LDOS are corresponding to total LDOS of per atom at different atomic positions of crystal structures of the inserts, respectively.

indicating additional electronic transfer channels. Therefore, conductivities are gradually increased in the sequence of 3D-(4,0) or 3D-(6,0)→3D-(5,0) or 3D-(9,0)→3D-(7,0)→3D-(8,0) carbons. The tunable conductivity is another unique feature for 3D nanotube polymers compared with those of graphite and graphene. These distinctive electronic properties of 3D nanotube polymers indicate the potential applications in optical or electronic nanodevices.

Young's Moduli. One-dimensional carbon nanotubes are highly stiff in their axial directions. The theoretically and experimentally confirmed axial Young's moduli of the nanotubes are insensitive to tube radius or chirality, and have values of around 1 TPa, which are consistent with the in-plane isotropic Young's moduli of a graphene sheet.[47−51] However, tubes appear extraordinarily flexible and elastic in their radial directions. The experimentally obtained radial moduli of multiwalled nanotubes are only in the range of 0.3−4 GPa and 9.7−80.0 GPa.[52,53] Compared with 1D nanotubes, our calculated axial Young's moduli (Table 1) of 3D-(*n*, 0) and 3D-(*n*, *n*) carbons can reach 1 TPa, and their radial Young's moduli are higher with hundred GPa or even 1 TPa units. Consequently, the newly designed 3D nanotube polymers cannot only retain the superior mechanical performance in axial directions of nanotubes, but also give great enhanced reinforcements in their radial directions through sp^3 bond buckling.

Tensile Strength. The sp^2 hybridized C−C bond in graphene is very strong chemical bond. The experimental tensile strength values of defect-free graphene and carbon nanotubes reach 130 ± 10 and 150 ± 45 GPa, respectively.[54,55] Today, the ideal tensile strength of a crystal can be accurately determined by first-principles calculations.[56−58] Recently, we presented a simple and semiempirical model to calculate the theoretical tensile strength, and the values can be reproduced from first-principles calculations.[59] Our calculated tensile strength of graphene in the zigzag ⟨10⟩ direction and (10, 0) nanotubes in the axial direction are 162.7 and 161.0 GPa, respectively.[59]

In the current study, the theoretical tensile strength in a specified direction is microscopically determined

by bond strength and broken bond number (bond density). Weak bond strength and small bond density would result in low tensile strength, and vice versa. The bond strength of i—j bond is proposed to be equal to the maximum tensile force F_{ij} unbinding i—j bond, and proved to be exclusively dependent on two microscopic parameters: bond length d_{ij} and effectively bonded valence electron (EBVE) number n_{ij}. Here n_{ij} can be calculated from the expression: $n_{ij} = n_i n_j/(n_i^2 + n_j^2)^{1/2}$, $n_i = Z_i/N_i$, $n_j = Z_j/N_j$, where Z_i and Z_j are the valence electron numbers of atom i and j, respectively, and N_i and N_j are the coordination numbers of atoms i and j, respectively. F_{ij} is calculated to follow the formula: $F_{ij}(N) = 6.6 \times 10^{-10}\ d_{ij}^{-1.32} \exp(3.7 n_{ij})$. Finally, the theoretical tensile strength σ_{hkl} of a crystal in the $\langle hkl \rangle$ direction can be calculated according to the formula: $\sigma_{hkl}^{theor}(Pa) = F_{ij} S_{hkl}$, where S_{hkl}, in units of m^{-2}, is the number of the broken bonds per unit area on the (hkl) plane, which has the lowest bond density.

On the basis of our model, the theoretical tensile strengths of 3D nanotube polymers were calculated (see Table 1, Supporting Information, Table S3, and Table S4). In the axial directions, the 3D-(6,0) carbon has the lowest tensile strength of 53.10 GPa, and whereas the 3D-(8,0) carbon has the highest strength of 177.19 GPa. In the radial directions, the 3D-(8,0) carbon has the lowest tensile strength of 26.70 GPa, whereas the 3D-(4,4) carbon has the highest strength of 115.09 GPa. The three factors that cause variations in tensile strength are n_{ij}, d_{ij}, and S_{hkl}. For bond I, formed by two sp^3 hybridized carbon atoms (red atoms in Figure 6), $n_{ij} = 0.707$; for bond II, formed by two sp^2 hybridized atoms (green or olive atoms), $n_{ij} = 0.943$; for bond III, formed by sp^3 bonded (red atom) and sp^2 bonded (green atom) atoms, $n_{ij} = 0.800$. The length sequence of the three types of bonds is $d_I > d_{III} > d_{II}$. Therefore, bond II is the strongest, bond III is moderate, and bond I is relatively weak, based on n_{ij} and d_{ij}. The isosurfaces of electron density differences in Figure 6 are a good indication of bond strength. As seen in Figure 6, bond II (in blue square brackets) has the highest electron density, and bond I (in blue ovals) has the lowest value, which is consistent with our theory. Aside from bond strength, the number of broken bonds per unit area on the (hkl) plane is also pivotal to the tensile strength of crystals in the $\langle$hkl$\rangle$ direction. The lowest bond density on the (hkl) plane usually determines the maximal tensile strength. The axial tensile strength σ_a of the 3D-(6,0) carbon (Figure 6a) and the radial tensile strength σ_r of the 3D-(8,0) carbon (Figure 6d) correspond to breaks of the weaker bond I with low bond density, which accounts for their low tensile strength. However, σ_a of the 3D-(8,0) carbon (Figure 6c) corresponds to the breaks of bond I and II with high bond density, which is responsible for its high σ_a. For the 3D-(4,4) carbon, the broken bonds are strongest bond II in the radial directions (Figure 6b), resulting in high σ_r.

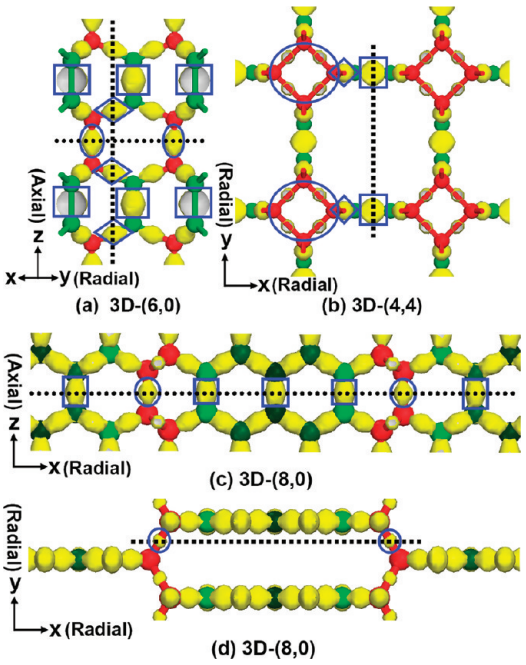

Figure 6. Isosurfaces of electron density differences (yellow) of 3D-(6,0), 3D-(8,0), and 3D-(4,4) carbons in their axial or radial directions. The green, red, olive, and dark olive atoms are corresponding to different atomic positions of crystal structures. Red atoms are sp^3 hybridized, and green (or olive) atoms are sp^2 hybridized. Different electron density differences between atoms are shown in blue square brackets, ovals, and rhombus, respectively.

Hardness. The bulk and shear moduli of the carbon allotropes (Table 1) were also calculated according to the Voigt-Reuss-Hill rule.[60−62] The 3D nanotube polymers have significantly higher bulk moduli B and shear moduli G than corresponding nanotubes (see Supporting Information, Table S2). In our microscopic theoretical model of hardness, the hardness of covalence-dominant crystals is dependent not only on the bond length, bond density, and ionicity of the bond, but also on the metallicity of the bond and orbital form in the crystal structure.[63−65] Using this model, the Vickers hardness (H_v) values of the carbon allotropes were estimated.

The calculated formulas are as follows: $H_v = 350 N_e^{2/3} e^{-1.191 f_i}/d^{2.5}$ for semiconducting carbon phases, and $H_v = 350 N_e^{2/3} e^{-1.191 f_i - 32.2 f_m^{0.55}}/d^{2.5}$ for metallic carbon phases. N_e is the electron density, calculated by $N_e = n_c Z_c/V$, where n_c is the number of C atoms in one unit cell, Z_c is the valence electron number of C atoms, and V is the volume of a unit cell; f_i is the Phillips ionicity of the C—C bond, which is equal to 0 here; f_m is a factor of metallicity, calculated by $f_m = 0.026 D_F/n_e$, where D_F is the total density of states of a unit cell at the Fermi level, and n_e is the total number of the valence electrons in unit cell; d is the average C—C bond length, calculated by

$d = \sum_j N^j d^j / \sum_j N^j$, where N^j is the number of j bond in the unit cell, and d^j is the j bond length.

The calculated hardness values are listed in Table 1 and Table S5 (Supporting Information). 3D nanotube polymers, except 3D-(9,0) carbon with a hardness value of 36.0 GPa, are all superhard. The 3D-(3,0), 3D-(2,2), 3D-(3,3), and 3D-(4,4) carbons are semiconducting superhard, and the 3D-(4,0), 3D-(5,0), 3D-(6,0), 3D-(7,0), 3D-(8,0), and 3D-(6,6) carbons are conducting superhard. They can meet different needs for industry applications, such as cutting tools, abrasives, and coatings.

Ductility. It is well-known that tetrahedral sp^3-hybridized bonds cannot hold large deformations and abruptly break down with stress, whereas sp^2-hybridized bonds can sustain large distortions through the out-of-plane bending. Consequently, sp^3-hybridized diamond, hexagonal diamond [*viz.* 3D-(3,0) carbon], and 3D-(2,2) carbon are extremely brittle. In comparison, nine other sp^2- and sp^3-hybridized 3D nanotube polymers are more ductile. The quantitative criterion for determining ductile or brittle materials is the *B*/*G* ratio. A high (low) *B*/*G* value is often associated with ductility (brittleness), and the critical value is about 1.75.[66] The *B*/*G* values (Table 1) of 3D-(9,0), 3D-(4,4), and 3D-(6,6) carbons are 2.05, 1.98, and 2.08, indicating that they are ductile carbon materials. This high ductility endows 3D nanotube polymers with the capability of resisting large strains without fracturing.

CONCLUSIONS

In summary, eight novel sp^2- and sp^3-hybridized 3D nanotube polymers were predicted. These 3D nanotube polymers are derived from zigzag (*n*, 0) and armchair (*n*, *n*) carbon nanotubes composed of interconnected identical parallel-oriented nanotubes. They are all more stable than C_{60} fullerene at ambient conditions. Among them, 3D-(4,0), 3D-(5,0), 3D-(7,0), 3D-(8,0), and 3D-(3,3) carbons have lower energies than their corresponding nanotube parents, and synthesizing them through the treatment of high-energy carbon nanotubes and/or fullerenes appears to be promising.

Compared with their corresponding 1D nanotube parents, 3D nanotube polymers have distinctive electronic properties. Among them, 3D-(3,3) and 3D-(4,4) carbons are semiconducting, 3D-(4,0) carbon is linearly conductive, 3D-(5,0), 3D-(6,0), 3D-(7,0), and 3D-(8,0) carbons have planar conductivity, and 3D-(9,0) and 3D-(6,6) carbons are 3D conducting. Conductivities are gradually increased in the sequence of 3D-(4,0) or 3D-(6,0)→3D-(5,0) or 3D-(9,0)→3D-(7,0)→3D-(8,0) carbons. The unusual conducting directions and tunable conductivity make 3D-nanotubes polymers amount to something in optical or electronic nanodevices.

Furthermore, 3D nanotube polymers have excellent mechanical performances, including high Young's moduli, high tensile strength, ultrahigh hardness, and good ductility. Their axial Young's moduli are comparable with those of 1D nanotubes, which can reach 1 TPa, and their radial Young's moduli are clearly higher than those of nanotubes with hundreds of GPa or even 1 TPa units. Similar to their Young's moduli, their radial tensile strength σ_r also show a large increase because of the buckling of the sp^3 bonds. Using our microscopical model, the tensile strength and Vickers hardness of the polymers were estimated. Eight polymers, except the 3D-(9,0) carbon, were all superhard. Through analysis of the *B*/*G* ratio, it can be concluded that these polymers are more ductile than diamond due to their flexional sp^2-hybridized bonds. Thereinto, 3D-(9,0), 3D-(4,4), and 3D-(6,6) carbons are ductile materials.

Another notable property is the low density of these polymers, which indicates their potential use as hydrogen-storage materials, shape-selective catalysts, molecular sieves, and absorbents. Therefore, 3D nanotube polymers with distinctive electronic properties, high Young's moduli, high tensile strength, ultrahigh hardness, good ductility, and low densities may be potentially applied in a variety of fields.

METHODS

Searching for Low-Energy Crystal Structures. The *ab initio* particle-swarm optimization (PSO) algorithm (CALYPSO code) within the evolutionary scheme has been designed to search for the carbon structures possessing the lowest (free) energy.[37−39] The most significant feature of the code is the capability of predicting the stable structure at given pressure and temperature conditions with only the knowledge of the chemical composition. On the way to the global minimum, the algorithm gradually focus a search on the most promising areas of the (free) energy landscape, thus giving an enhanced (though not exhaustive) sampling of low-energy structures. The underlying structure relaxations were performed using density functional theory within the local density approximation (LDA) as implemented in the Vienna *ab initio* simulation package (VASP code).[67] Herein we performed variable-cell structure prediction simulations using the above evolutionary methodology for carbon containing 2, 4, 6, 8, 10, 12, 14, and 16 atoms in the cell at the ground state, respectively.

Constructions of Periodic Carbon Nanotubes. Nanotubes can be constructed in *Materials Studio* soft.[68] A nanotube is formed by rolling a graphene sheet into a cylinder. The building process can be logically separated in two parts: determining the positions of the atoms and establishing the bonding pattern in the nanotube. Atomic positions are defined unambiguously by the chiral vector and by the bond length (1.42 Å) of the ideal graphene sheet. The actual bonds are created between the nanotube atoms based on the settings of the connectivity options for bond calculations.

Periodic nanotubes, indicate that a periodic lattice, comprising one repeat unit of a single-wall nanotube, were built. A standard hexagonal packing arrangement of nanotubes were

used, in which the $a = b$ dimension is determined by the nanotube diameter plus two half the graphite interlayer separation. This means that the nanotubes are at approximately the same separation as the layers in graphite, 3.347 Å. Using the method, we built the crystal structures of periodic zigzag (n, 0) and armchair (n, n) carbon nanotubes.

Structural Optimizations and Property Predictions. Structural optimizations and property predictions were carried out using the density functional theory (DFT) within the ultrasoft pseudopotentials, as implemented in the CASTEP code.[68] The cutoff energy of 310 eV was used for the plane wave basis set. The electron−electron exchange interaction is described by the exchange-correlation function of Ceperley and Alder, as parametrized by Perdew and Zunger (CA-PZ) of the local-density approximation (LDA).[69,70] A k-point separation (0.04 $Å^{-1}$) corresponding to fine quality level was used to generate the k-point grid, resulting from the Monkhorst-Pack grid parameters.[71] The Monkhorst-Pack grids for primitive cell optimizations of 3D-(3,0), 3D-(4,0), 3D-(5,0), 3D-(6,0), 3D-(7,0), 3D-(8,0), 3D-(9,0), 3D-(2,2), 3D-(3,3), 3D-(4,4), 3D-(6,6) carbons are $12 \times 12 \times 6$, $12 \times 7 \times 10$, $10 \times 10 \times 6$, $6 \times 6 \times 6$, $10 \times 10 \times 6$, $11 \times 6 \times 9$, $4 \times 4 \times 6$, $12 \times 12 \times 8$, $11 \times 11 \times 5$, $5 \times 5 \times 10$, $4 \times 4 \times 10$, respectively. The Monkhorst-Pack grids for electronic density of states (DOS)/local density of state (LDOS) calculations of 3D-(3,0), 3D-(4,0), 3D-(5,0), 3D-(6,0), 3D-(7,0), 3D-(8,0), 3D-(9,0), 3D-(2,2), 3D-(3,3), 3D-(4,4), 3D-(6,6) carbons are $12 \times 12 \times 6$, $4 \times 10 \times 6$, $10 \times 3 \times 6$, $6 \times 6 \times 6$, $9 \times 2 \times 6$, $2 \times 9 \times 6$, $4 \times 4 \times 6$, $6 \times 6 \times 10$, $4 \times 10 \times 5$, $5 \times 5 \times 10$, $4 \times 4 \times 10$, respectively. The structural optimization was performed until the energy change of per atom was less than 5×10^{-6} eV, the forces on atoms were less than 0.01 eV/Å, and all the stress components were less than 0.02 GPa. Then, band structures were calculated along the high symmetrical k points of Brillouin Zone, and corresponding primitive cell were used. To find out the electronic environment throughout the unit cell, the whole unit cell was used to calculate electronic DOS, LDOS and isosurfaces of electron density differences. In addition, we also calculated their elastic constants, bulk moduli, and shear moduli.

Acknowledgment. This work was supported by NSFC (Grant Nos. 50821001, 91022029, and 11174152), FANEDD (Grant No. 2007B36), NBRPC (Grant No. 2011CB808205), and by the Science Foundation of Yanshan University for the Excellent Ph. D. Students (Grant No. YSUSF201101).

Supporting Information Available: Crystal structure information (Table S1), elastic constants (Table S2), calculated axial and radial tensile strength with related parameters (Table S3 and S4), calculated bond parameters and Vickers hardness (Table S5), and the coordinates of the high symmetry points in reciprocal space for calculated band structures (Table S6) of 3D nanotube polymers. Top views of (n, 0) carbon nanotubes along their axial directions are shown in Figure S1. Band structure, electron orbits, and LDOS of semimetallic 3D-(6, 0) carbon are shown in Figure S2. The sp^2 hybridized bonds (yellow bonds) and sp^3 hybridized bonds (gray bonds) in crystal structures are shown in Figure S3. In addition, the calculated elastic constants (GPa), bulk and shear moduli (GPa) of graphite and the carbon nanotubes including (6,0), (7,0), (8,0), (9,0), (4,4), (6,6) nanotubes are listed in Table S2. This material is available free of charge *via* the Internet at http://pubs.acs.org.

REFERENCES AND NOTES

1. Bundy, F. P.; Bovenkerk, H. P.; Strong, H. M.; Wentorf, R. H., JR. Diamond-Graphite Equilibrium Line from Growth and Graphitization of Diamond. *J. Chem. Phys.* **1961**, *35*, 383–391.
2. Yagi, T.; Utsumi, W.; Yamakata, M.; Kikegawa, T.; Shimomura, O. High-Pressure *in Situ* X-ray-Diffraction Study of the Phase Transformation from Graphite to Hexagonal Diamond at Room Temperature. *Phys. Rev. B* **1992**, *46*, 6031–6039.
3. Kroto, H. W.; Heath, J. R.; O'Brien, S. C.; Curl, R. F.; Smalley, R. E. C_{60}:Buckminsterfullerene. *Nature* **1985**, *318*, 162–163.
4. Heath, J. R.; Zhang, Q.; O'Brien, S. C.; Curl, R. F.; Kroto, H. W.; Smalley, R. E. The Formation of Long Carbon Chain Molecules during Laser Vaporization of Graphite. *J. Am. Chem. Soc.* **1987**, *109*, 359–363.
5. Voevodin, A. A.; Laube, S. J. P.; Walck, S. D.; Solomon, J. S.; Donley, M. S.; Zabinski, J. S. Pulsed Laser Deposition of Diamond-like Amorphous Carbon Films from Graphite and Polycarbonate Targets. *J. Appl. Phys.* **1995**, *78*, 4123–4130.
6. Friedmann, T. A.; McCarty, K. F.; Barbour, J. C.; Siegal, M. P.; Dibble, D. C. Thermal Stability of Amorphous Carbon Films Grown by Pulsed Laser Deposition. *Appl. Phys. Lett.* **1996**, *68*, 1643–1645.
7. Novoselov, K. S.; Geim, A. K.; Morozov, S. V.; Jiang, D.; Zhang, Y.; Dubonos, S. V.; Grigorieva, I. V.; Firsov, A. A. Electric Field Effect in Atomically Thin Carbon Films. *Science* **2004**, *306*, 666–669.
8. Novoselov, K. S.; Geim, A. K.; Morozov, S. V.; Jiang, D.; Katsnelson, M. I.; Grigorieva, I. V.; Dubonos, S. V.; Firsov, A. A. Two-Dimensional Gas of Massless Dirac Fermions in Graphene. *Nature* **2005**, *438*, 197–200.
9. Liu, P.; Cui, H.; Yang, G. W. Synthesis of Body-Centered Cubic Carbon Nanocrystals. *Cryst. Growth Des.* **2008**, *8*, 581–586.
10. Liu, P.; Cao, Y. L.; Wang, C. X.; Chen, X. Y.; Yang, G. W. Micro- and Nanocubes of Carbon with C_8-like and Blue Luminescence. *Nano Lett.* **2008**, *8*, 2570–2575.
11. Marques, L.; Hodeau, J.-L.; Nunez-Regueiro, M.; Perroux, M. Pressure and Temperature Diagram of Polymerized Fullerite. *Phys. Rev. B* **1996**, *54*, R12633–R12636.
12. Brazhkin, V. V.; Lyapin, A. G.; Popova, S. V.; Klyuev, Yu. A.; Naletov, A. M. Mechanical Properties of the 3D Polymerized, sp^2−sp^3 Amorphous, and Diamond-Plus-Graphite Nanocomposite Carbon Phases Prepared from C_{60} under High Pressure. *J. Appl. Phys.* **1998**, *84*, 219–226.
13. Blank, V. D.; Buga, S. G.; Dubitsky, G. A.; Serebryanaya, N. R.; Popov, M. Y.; Sundqvist, B. High-Pressure Polymerized Phases of C_{60}. *Carbon* **1998**, *36*, 319–343.
14. Yamanaka, S. J.; Kubo, A.; Inumaru, K.; Komaguchi, K. J.; Kini, N. S.; Inoue, T.; Irifune, T. Electron Conductive Three-Dimensional Polymer of Cuboidal C_{60}. *Phys. Rev. Lett.* **2006**, *96*, 076602.
15. Tonkov, E. Y.; Ponyatovsky, E. G. *Phase Transformations of Elements under High Pressure*; CRC: Boca Raton, FL, 2005; pp 86−89.
16. Kumar, R. S.; Pravica, M. G.; Cornelius, A. L.; Nicol, M. F.; Hu, M. Y.; Chow, P. C. X-ray Raman Scattering Studies on C_{60} Fullerenes and Multiwalled Carbon Nanotubes under Pressure. *Diamond Relat. Mater.* **2007**, *16*, 1250–1253.
17. Wang, Z. W.; Zhao, Y. S.; Tait, K.; Liao, X. Z.; Schiferl, D.; Zha, C. S.; Downs, R. T.; Qian, J.; Zhu, Y. T.; Shen, T. D. A Quenchable Superhard Carbon Phase Synthesized by Cold Compression of Carbon Nanotubes. *Proc. Natl. Acad. Sci. U.S.A.* **2004**, *101*, 13699–13702.
18. Popov, M.; Kyotani, M.; Koga, Y. Superhard Phase of Single Wall Carbon Nanotube: Comparison with Fullerite C_{60} and Diamond. *Diamond Relat. Mater.* **2003**, *12*, 833–839.
19. Mao, W. L.; Mao, H.-K.; Eng, P. J.; Trainor, T. P.; Newville, M.; Kao, C.-C; Heinz, D. L.; Shu, J.; Meng, Y.; Hemley, R. J. Bonding Changes in Compressed Superhard Graphite. *Science* **2003**, *302*, 425–427.
20. Li, Q.; Ma, Y. M.; Oganov, A. R.; Wang, H. B.; Wang, H.; Xu, Y.; Cui, T.; Mao, H. K.; Zou, G. T. Superhard Monoclinic Polymorph of Carbon. *Phys. Rev. Lett.* **2009**, *102*, 175506.
21. Umemoto, K.; Wentzcovitch, R. M.; Saito, S.; Miyake, T. Body-Centered Tetragonal C_4: A Viable sp^3 Carbon Allotrope. *Phys. Rev. Lett.* **2010**, *104*, 125504.
22. Zhou, X.-F.; Qian, G. R.; Dong, X.; Zhang, L. X.; Tian, Y. J.; Wang, H. T. *Ab Initio* Study of the Formation of Transparent Carbon under Pressure. *Phys. Rev. B* **2010**, *82*, 134126.
23. Wang, J.-T.; Chen, C. F.; Kawazoe, Y. Low-Temperature Phase Transformation from Graphite to sp^3 Orthorhombic Carbon. *Phys. Rev. Lett.* **2011**, *106*, 075501.
24. Bucknum, M. J.; Castro, E. A. The Carbon Allotrope Hexagonite and Its Potential Synthesis from Cold Compression of

Carbon Nanotubes. *J. Chem. Theory Comput.* **2006**, *2*, 775–781.
25. Omata, Y.; Yamagami, Y.; Tadano, K.; Miyake, T.; Saito, S. Nanotube Nanoscience: A Molecular-Dynamics Study. *Phys. E* **2005**, *29*, 454–468.
26. Karfunkel, H. R.; Dressler, T. New Hypothetical Carbon Allotropes of Remarkable Stability Estimated by Modified Neglect of Diatomic Overlap Solid-State Self-Consistent Field Computations. *J. Am. Chem. Soc.* **1992**, *114*, 2285–2288.
27. Martoňák, R.; Laio, A.; Parrinello, M. Predicting Crystal Structures: The Parrinello-Rahman Method Revisited. *Phys. Rev. Lett.* **2003**, *90*, 075503.
28. Martoňák, R.; Laio, A.; Bernasconi, M.; Ceriani, C.; Raiteri, P.; Zipoli, F.; Parrinello, M. *Z. Kristallogr.* **2005**, *220*, 489–498.
29. Sun, J.; Klug, D. D.; Martoňák, R.; Montoya, J. A.; Lee, M.-S.; Scandolo, S.; Tosatti, E. High-Pressure Polymeric Phases of Carbon Dioxide. *Proc. Natl. Acad. Sci. U.S.A.* **2009**, *106*, 6077–6081.
30. Oganov, A. R.; Glass, C. W. Crystal Structure Pprediction using *ab Initio* Evolutionary Techniques: Principles and Applications. *J. Chem. Phys.* **2006**, *124*, 244704.
31. Glass, C. W.; Oganov, A. R.; Hansen, N. USPEX—Evolutionary Crystal Structure Prediction. *Comput. Phys. Commun.* **2006**, *175*, 713–720.
32. Oganov, A. R.; Chen, J. H.; Gatti, C.; Ma, Y. Z.; Ma, Y. M.; Glass, C. W.; Liu, Z. X.; Yu, T.; Kurakevych, O. O.; Solozhenko, V. L. Ionic High-Pressure Form of Elemental Boron. *Nature* **2009**, *457*, 863–867.
33. Ma, Y. M.; Eremets, M.; Oganov, A. R.; Xie, Y.; Trojan, I.; Medvedev, S.; Lyakhov, A. O.; Valle, M.; Prakapenka, V. Transparent Dense Sodium. *Nature* **2009**, *458*, 182–185.
34. Pickard, C. J.; Needs, R. J. High-Pressure Phases of Silane. *Phys. Rev. Lett.* **2006**, *97*, 045504.
35. Pickard, C. J.; Needs, R. J. Highly Compressed Ammonia Forms an Ionic Crystal. *Nat. Mater.* **2008**, *7*, 775–779.
36. Pickard, C. J.; Needs, R. J. Structure of Phase III of Solid Hydrogen. *Nat. Phys.* **2007**, *3*, 473–476.
37. Wang, Y. C.; Lv, J.; Zhu, L.; Ma, Y. M. Crystal Structure Prediction *via* Particle-Swarm Optimization. *Phys. Rev. B* **2010**, *82*, 094116.
38. Lv, J.; Wang, Y. C.; Zhu, L.; Ma, Y. M. Predicted Novel High-Pressure Phases of Lithium. *Phys. Rev. Lett.* **2011**, *106*, 015503.
39. Zhu, L.; Wang, H.; Wang, Y. C.; Lv, J.; Ma, Y. M.; Cui, Q. L.; Ma, Y. M.; Zou, G. T. Substitutional Alloy of Bi and Te at High Pressure. *Phys. Rev. Lett.* **2011**, *106*, 145501.
40. David, W. I. F.; Ibberson, R. M.; Matthewman, J. C.; Prassides, K.; Dennis, T. J. S.; Hare, J. P.; Kroto, H. W.; Taylor, R.; Walton, D. R. M. Crystal Structure and Bonding of Ordered C_{60}. *Nature* **1991**, *353*, 147–149.
41. Wang, J.-T.; Chen, C. F.; Wang, D.-S.; Mizuseki, H.; Kawazoe, Y. Phase Stability of Carbon Clathrates at High Pressure. *J. Appl. Phys.* **2010**, *107*, 063507.
42. Peng, L.-M.; Zhang, Z. L.; Xue, Z. Q.; Wu, Q. D.; Gu, Z. N.; Pettifor, D. G. Stability of Carbon Nanotubes: How Small Can They Be? *Phys. Rev. Lett.* **2000**, *85*, 3249–3252.
43. Zhao, X.; Liu, Y.; Inoue, S.; Suzuki, T.; Jones, R. O.; Ando, Y. Smallest Carbon Nanotube Is 3 Å in Diameter. *Phys. Rev. Lett.* **2004**, *92*, 125502.
44. Ouyang, M.; Huang, J.-L.; Cheung, C. L.; Lieber, C. M. Energy Gaps in "Metallic" Single-Walled Carbon Nanotubes. *Science* **2001**, *292*, 702–705.
45. Odom, T. W.; Huang, J.-L.; Kim, P.; Lieber, C. M. Atomic Structure and Electronic Properties of Single-Walled Carbon Nanotubes. *Nature* **1998**, *391*, 62–64.
46. Wang, X. L. Proposal for a New Class of Materials: Spin Gapless Semiconductors. *Phys. Rev. Lett.* **2008**, *100*, 156404.
47. Krishnan, A.; Dujardin, E.; Ebbesen, T. W.; Yianilos, P. N.; Treacy, M. M. J. Young's Modulus of Single-Walled Nanotubes. *Phys. Rev. B* **1998**, *58*, 14013–14019.
48. Lier, G. V.; Alsenoy, C. V.; Doren, V. V.; Geerlings, P. *Ab Initio* Study of the Elastic Properties of Single-Walled Carbon Nanotubes and Graphene. *Chem. Phys. Lett.* **2000**, *326*, 181–185.
49. Yao, N.; Lordi, V. Young's Modulus of Single-Walled Carbon Nanotubes. *J. Appl. Phys.* **1998**, *84*, 1939–1943.
50. Wong, E. W.; Sheehan, P. E.; Lieber, C. M. Nanobeam Mechanics: Elasticity, Strength, and Toughness of Nanorods and Nanotubes. *Science* **1997**, *277*, 1971–1975.
51. Treacy, M. M. J.; Ebbesen, T. W.; Gibson, J. M. Exceptionally High Young's Modulus Observed for Individual Carbon Nanotubes. *Nature* **1996**, *381*, 678–680.
52. Yu, M. -F.; Kowalewski, T.; Ruoff, R. S. Investigation of the Radial Deformability of Individual Carbon Nanotubes under Controlled Indentation Force. *Phys. Rev. Lett.* **2000**, *85*, 1456–1459.
53. Shen, W. D.; Jiang, B.; Han, B. S.; Xie, S. -S. Investigation of the Radial Compression of Carbon Nanotubes with a Scanning Probe Microscope. *Phys. Rev. Lett.* **2000**, *84*, 3634–3637.
54. Lee, C. G.; Wei, X. D.; Kysar, J. W.; Hone, J. Measurement of the Elastic Properties and Intrinsic Strength of Monolayer Graphene. *Science* **2008**, *321*, 385–388.
55. Demczyk, B. G.; Wang, Y. M.; Cumings, J.; Hetman, M.; Han, W.; Zettl, A.; Ritchie, R. O. Direct Mechanical Measurement of the Tensile Strength and Elastic Modulus of Multiwalled Carbon Nanotubes. *Mater. Sci. Eng. A* **2002**, *334*, 173–178.
56. Roundy, D.; Cohen, M. L. Ideal Strength of Diamond, Si, and Ge. *Phys. Rev. B* **2001**, *64*, 212103.
57. Ogata, S.; Shibutani, Y. Ideal Tensile Strength and Band Gap of Single-Walled Carbon Nanotubes. *Phys. Rev. B* **2003**, *68*, 165409.
58. Liu, F.; Ming, P. B.; Li, J. *Ab initio* Calculation of Ideal Strength and Phonon Instability of Graphene under Tension. *Phys. Rev. B* **2007**, *76*, 064120.
59. Guo, X. J.; Wang, L.-M.; Xu, B.; Liu, Z. Y.; Yu, D. L.; He, J. L.; Wang, H.-T.; Tian, Y. J. Unbinding Force of Chemical Bonds and Tensile Strength in Strong Crystals. *J. Phys.: Condens. Matter* **2009**, *21*, 485405.
60. Voigt, W. *Lehrburch der Kristallphysik*; Teubner: Leipzig, Germany, 1928.
61. Reuss, A. *Z. Angew. Math. Mech.* **1929**, *9*, 49.
62. Hill, R. *Proc. Phys. Soc. (London)* **1952**, *65*, 350.
63. Gao, F. M.; He, J. L.; Wu, E. D.; Liu, S. M.; Yu, D. L.; Li, D. C.; Zhang, S. Y.; Tian, Y. J. Hardness of Covalent Crystals. *Phys. Rev. Lett.* **2003**, *91*, 015502.
64. He, J. L.; Wu, E. D.; Wang, H. T.; Liu, R. P.; Tian, Y. J. Ionicities of Boron–Boron Bonds in B_{12} Icosahedra. *Phys. Rev. Lett.* **2005**, *94*, 015504.
65. Guo, X. J.; Li, L.; Liu, Z. Y.; Yu, D. L.; He, J. L.; Liu, R. P.; Xu, B.; Tian, Y. J.; Wang, H. T. Hardness of Covalent Compounds: Roles of Metallic Component and *d* Valence Electrons. *J. Appl. Phys.* **2008**, *104*, 023503.
66. Pugh, S. F. Relations between the Elastic Moduli and the Plastic Properties of Polycrystalline Pure Metals. *Philos. Mag.* **1954**, *45*, 823–843.
67. Kresse, G.; Furthmüller, J. Efficient Iterative Schemes for *ab Initio* Total-Energy Calculations Using a Plane-Wave Basis Set. *Phys. Rev. B* **1996**, *54*, 11169.
68. *Materials Studio*, version 4.1; Accelrys Inc.: San Diego, CA, 2006.
69. Ceperley, D. M.; Alder, B. J. Ground State of the Electron Gas by a Stochastic Method. *Phys. Rev. Lett.* **1980**, *45*, 566.
70. Perdew, J. P.; Zunger, A. Self-Interaction Correction to Density-Functional Approximations for Many-Electron Systems. *Phys. Rev. B* **1981**, *23*, 5048.
71. Monkhorst, H. J.; Pack, J. D. Special Points for Brillouin-zone Integrations. *Phys. Rev. B* **1976**, *13*, 5188.